Advanced quantification of the carbide spacing and correlation with dimple size in a high-strength medium carbon martensitic steel

Anne-Françoise Gourgues-Lorenzon, Frank Tioguem, Franck N'Guyen, Matthieu Mazière, Franck Tankoua, André Galtier, Anne-Françoise Gourgues

Advanced quantification of the carbide spacing and correlation with dimple size in a high-strength medium carbon martensitic steel

Frank TIOGUEM[1, 2a], Franck N'GUYEN[1], Matthieu MAZIERE[1],

Franck TANKOUA[2b], André GALTIER[2], Anne-Françoise GOURGUES LORENZON[1]

[1] MINES ParisTech – PSL University – Centre des Matériaux UMR CNRS 7633, BP 87 – 91003 Evry cedex, France.

[2] Ascometal France Holding– Centre de Recherche CREAS, BP 70045 avenue de France, 57301 Hagondange, France.

[a] Now at Framatome, 6 allée Jean Perrin 71200 Le Creusot, France

[b]Now at CEA Saclay, 91191 Gif-sur-Yvette Cedex, France

Corresponding author: anne-francoise.gourgues@mines-paristech.fr

Declaration of interests: none.

Abstract

Interparticle spacing in materials science is a key parameter controlling ductile fracture. It is generally evaluated as the distance between particle centers of mass. High strength medium carbon martensitic steels contain a high density of carbides, whose size is non-negligible with respect to the distance between them. Current microstructural quantification methods do not take the shape of analyzed particles into account, thus being not necessarily relevant to materials containing a high density of particles that trigger void nucleation and ductile fracture.

This work reports on the potency of a simple full field particle quantification method based on a watershed algorithm that takes the shape and spatial distribution of particles into account. Three microstructures were produced by heat treating a hot-rolled 40CrMo4 steel bar. Cementite carbide populations of each microstructure were quantified using carbon extractive replicas, conventional image processing and application of the developed algorithm. A comparison of results from a full field Voronoi tiling algorithm revealed pronounced differences in the shape of distributions. The watershed-based method was shown to allow efficient interpretation of the relationships between carbide distribution and ductile fracture features.

Keywords: watershed; Voronoi; high strength steel; carbide distribution; ductile fracture; dimple quantification.

1. Introduction

Quenched and tempered steel grades are commonly used for manufacturing of severely loaded machine parts, such as those used in *off-shore* drilling. They are continuously being improved to combine high strength (typically, yield strength >1000 MPa) with good ductility (typically, 10-15%). These properties rely on a martensitic microstructure (sometimes associated to lower bainite) containing a high fraction of fine carbides, (e.g., [1-7]). The volume fraction of carbide is typically more than 4 vol% for steels containing 0.4 wt% carbon. On the other hand, a high density of hard carbides in a strong martensitic matrix may limit the impact toughness in the ductile fracture domain by increasing the sensitivity to strain localization and void nucleation [8].

Establishing a quantitative link between carbide (and, more generally, inclusion) spacing and ductile fracture in these materials requires quantification of relevant microstructural parameters. In particular, the nearest-neighbor distance (NND) between particles has to be characterized in a way relevant to the physical mechanisms of ductile fracture. Such investigations have been reported in non-ferrous alloys [9-10]. As for steels, sulfide and oxide inclusions that lead to the first formed population of cavities have been quantified [8, 11-15]. In all these materials, the volume fraction of inclusions was low (typically, less than 1%). In addition, the shape and spatial distribution of coarse particles can influence void nucleation and growth mechanisms and kinetics, as reported in e.g. [8, 15-20]. Many high strength steels contain carbides as strengthening particles. In addition to inclusion-matrix decohesion, carbides have been reported to act in the ductile fracture process in 4340-type quenched and tempered steels [11, 21] as well as in other high strength steels [8, 12, 13, 22, 23]. As reported in these studies, primary cavities nucleated at inclusions such as sulfides but final fracture was driven by the later development of cavities at carbides.

As already shown in [1] and as will be illustrated in the present work, the size of carbides in medium-carbon martensitic steels may equal the distance between particles and thus, the size of the matrix ligaments between voids nucleated from them. Several approaches have been reported to evaluate particle spacing in alloys. Some of them directly use the volume fraction of particles to assess the ratio of particle size to particle spacing. To this aim, they generally assumed a homogeneous distribution of particles of uniform size [10]. So-called 'counting' methods use empirical formulae to convert point counts into distances (e.g., in [1, 8, 9, 12, 14, 24, 25]). As for carbide-induced ductile fracture of higher carbon and Cr-Ni 300M maraging steels, Curry and Pratt [8] and Hippsley and Druce [12] determined the mean spacing between particles considered as obstacles to moving dislocations, D_s. They counted the number of inclusions per unit area, N_a, then estimated the average center-to-center NND [26] using the following equation [24]:

$$D_s = 1.18{N_a}^{-0.5} \quad (1)$$

The area fraction of carbide particles being elevated (more than 4%) in the present work, the following Eq. 2 derived from [27] was also used to estimate D_s. In Eq. 2, f is the volume fraction of particles and N_c is the number of carbides intersecting a unit length:

$$D_s = {}^{1}/_{N_c}\,({}^{3\pi f}/_{8})^{0.5} \quad (2)$$

So-called 'full field' processes extract morphological information from micrographs, especially, about the shape and spatial arrangement of particles. In a bainitic SA508 (16Mn5NiMo) steel, Lee *et al.* [28] used image analysis measurements of minor axis, major axis and aspect ratio of more than 1400 carbides. Then, the carbides were sorted by their size. Only those larger than a certain size, being considered as active, were retained for

point counting; the NND, Δ, between those carbides was estimated by the following expression [29], also reported in [24, 26]:

$$\Delta = 0.5{N_a}^{-0.5} \quad (3)$$

The Voronoi tiling algorithm, developed since the 1970s is largely used as a numerical, full field analysis tool [15, 30-31]. This method consists in partitioning the observed plane into subsets - cells hereafter - resulting from flooding, from the center of mass of a distribution of objects, over the whole plane [32]. In this method, the center of mass of each particle is assumed to be representative of that particle. By using the Euclidian distance, the Voronoi cell associated to a given center of mass (*M*) is defined as the set of points, in the plane, that are closer to point *M* than to any other center of mass. Two centers of mass are nearest-neighbors if, and only if their associated Voronoi cells share a common edge. That common edge is, in fact, a portion of the perpendicular bisector of these two centers of mass. Any vertex is located at the same distance from at least three centers of mass. Statistical analysis gives possible estimates of the interparticle spacing distribution as the Voronoi cell size distribution [32] or from the distribution of Euclidian distances between nearest-neighbor centers of mass in the plane. Both point counting and Voronoi-based techniques have some limitations, one of which being not taking the shape of particles accurately into account.

Besides continuum damage [33] and data science approaches (e.g. [34]), most of ductile fracture modelling reported up to now adopted a local, micromechanical approach of the classical three stages, namely, void nucleation, growth and coalescence [35], as detailed below. Particle-induced strengthening of high-strength alloys creates obstacles to dislocation motion. During plastic deformation, dislocation pile-up at hard particles eventually leads to high interfacial stresses at and high internal stresses in the particles [9, 36-39]. Combined to a given applied stress state and plastic strain, this leads to void nucleation [8, 10-12, 16, 18, 36, 39, 40]. Void growth is driven by plasticity mechanisms that can be modelled either explicitly [41] of in the framework of the mechanics of porous media [42]. Microstructural features that influence initial void shape, plastic constraints by neighboring hard particle, and plastic flow anisotropy have been reported to influence this stage (e.g., [15, 43, 44]). Ductile fracture eventually occurs by void coalescence, which involves deformation and fracture of matrix ligaments located between voids. It has early been related to some local exhaustion of strain hardening [45]. In the so-called void impingement mechanism, coalescence occurs by matrix necking between voids nucleated from coarse particles or inclusions [36, 39]. In the so-called void sheeting mechanism, strain localization between primary voids triggers the nucleation and coalescence of secondary voids from smaller particles (such as carbides in high strength steels) [8, 12-14, 46]. The competition between these two coalescence mechanisms depends on the local stress-strain state [11, 15, 21, 23, 40, 44, 46-48]. It also depends on microstructural features such as inclusion size, orientation and spatial distribution [15, 44]. In the case of a dense distribution of particles such as in medium-carbon, high strength steels, it is important to clearly determine the effective *edge-to-edge* spacing between such particles, as an indicator of ligament geometry. To the authors' knowledge, such *experimental* determination, combined to quantitative analysis of ductile fracture surfaces, has scarcely been reported yet. Only [11, 25] subtracted the size of particles from the center-to center NND to get an estimate of edge-to-edge NNDs. Full-field numerical simulations of an elastic-plastic matrix containing particles (or voids) used the finite element method. They focused on the effect of stress state (in particular, stress triaxiality) and strain localization on the coalescence mechanism and kinetics. To this aim, the authors assumed either a periodic array of cavities [41] or of

sets of inclusions [19] or a one-cavity [10] or two-cavity problem [47], most of them for rather simple cavity geometry (ellipsoids or infinite cylinders).

In the present work, a full field image analysis method based on the watershed is proposed to quantify the carbide spacing distribution in a medium carbon, high strength steel intended for drilling applications. This method can be readily used for materials having a significant area fraction of particles (typically, several percent) and could be extended to three-dimensional analysis. It allows estimation of the NND between carbide particles while taking the combination of their shape and spatial distribution into account. The output is an edge-to-edge particle spacing distribution; it is used to enrich statistical analysis of the microstructure and of its influence on the ductile fracture process. Results from the proposed method are compared with those obtained by the conventional Voronoi tiling algorithm. The relevance of these measurements to the analysis of experimental ductile fracture data is also assessed.

2. Materials, experimental methods and observations

2.1. Materials

The studied steel was provided as a hot-rolled bar of 90 mm in radius with the chemical composition reported in Table 1. The level of sulfur was tuned to allow easy machining of parts. In the as-received state, the bar had been austenitized at 875°C and water quenched, tempered at 600°C and oil quenched (Material A, hereafter). Blanks were taken at 25 mm from the side surface of the as-received bar and exhibited a homogeneous microstructure. The average parent austenite grain size was estimated to 22 μm by an image analysis method after nital etching. Inclusion analysis showed MnS and Al_2O_3 particles aligned along the bar axis. In order to keep a similar martensite matrix microtexture while varying the carbide precipitation state, an additional tempering at either 665°C or 720°C was applied to blanks cut from Material A (Table 2). The resulting microstructures are respectively denoted Materials B and C, hereafter. Vickers micro-hardness was measured with 300g load and a dwell time of 10s. About 50 indents were realized for each material. As reported in Table 2, Material A was harder than Material B and Material C. The volume fraction of carbide predicted by equilibrium calculations (TCFE7 database, 700°C) is 0.047.

C	Mn	Si	Cr	Ni	Mo	Cu	P	S	Al	Fe
0.40	1.14	0.27	1.25	0.20	0.32	0.11	0.01	0.006	0.02	Bal.

Table 1: Chemical composition of the studied steel (wt. %)

Material	A	B	C
Heat treatment	Austenitized at 875°C for 1,500s (25 min), water quenched and tempered at 600°C for 10,800s (3h), oil quenched	Cut from Material A, then tempered at 690°C for 3,600s (1h) and oil quenched	Cut from Material A, then tempered at 720°C for 14,400s (4h) and oil quenched
Micro-hardness $HV_{0.3}$	344±15	269±9	236±12
YS (MPa)	900±10	678±47	590±2
TS (MPa)	1050±7	835±28	748±8
UEl	0.060±0.001	0.086±0.002	0.104±0.006
TEl	0.16±0.001	0.21±0.008	0.22±0.020
RA	0.62±0.01	0.70±0.01	0.61±0.06

Table 2: Heat-treatment schedules, resulting hardness and tensile properties along the bar axis. YS: yield strength (0.2% proof stress); TS; tensile strength; UEl: maximum uniform elongation; TEl: tensile fracture elongation; RA: reduction of area at fracture.

2.2. Conventional microstructural characterization

To carry out metallographic analysis, samples were polished down to 1μm-grade diamond paste in the plane perpendicular to the bar axis, then etched with a 4% nital solution. This plane was selected because it was the macroscopic fracture plane of tensile specimens as described in section 2.4. The samples were either directly observed (so-called 'bulk samples') or used to prepare carbon extractive replicas. In this last case, etched surfaces were coated with 50-nm-thick carbon film by using an evaporator. This thickness was selected in order to keep carbides embedded in the thin carbon film and to minimize spatial distribution artefacts linked to displacement of carbide particles on the thin carbon film. Subsequently, the thin carbon films were released from the bulk samples by immersion in a 10% nital solution for 20 min. The microstructures and replicas of the three materials were observed using a Zeiss Sigma300 field emission gun scanning electron microscope (SEM). The operating parameters were as follows: High voltage 5 kV, aperture 60 μm and magnification 1 x 10^4. The bulk samples and replicas were respectively observed with in-lens secondary electron and backscattered electron imaging modes. At least 5 images of size 1024 × 700 pixels were taken per material for statistical analysis on replica micrographs with 0.01μm as pixel size.

Fig. 1 presents typical micrographs of bulk samples and of replicas of the three materials. The microstructure of the three materials was martensitic with traces of lower bainite. There were coarser, rod-like carbides in addition to elongated, finer carbides. These carbides were also observed on replica micrographs, In many instances, elongated carbides seemed to result from the coalescence of several smaller particles (see e.g. the bottom parts of Figs 1e and 1h). From place to place, large clusters of carbides were found in replicas but not in bulk samples; they probably stemmed from artefacts during replica preparation. These clusters were discarded from further analysis. In bulk samples, coarser carbides were mainly located at lath boundaries and at prior austenite grain boundaries while elongated

fine carbides were located inside laths. Transmission Electron Microscopy (TEM) analysis using selected area diffraction patterns showed that the carbide population was of the M_3C (cementite) type. Comparison with micrographs of bulk samples ensured that the replica fabrication process did not introduce artefacts in the spatial distribution of carbides, once carbide clusters had been discarded during image recording.

The equivalent circle diameter of coarser M_3C carbides was estimated by using the thresholding operations of ImageJ® software to separate them from the population of finer carbides; in fact, finer carbides were not found to be ductile void nucleation sites. More than 2×10^3 carbides were considered for each material with a minimum size threshold of 0.05 μm. The average equivalent circle diameter of measured carbides was respectively 0.08 μm, 0.09 μm, and 0.12 μm for Materials A, B, and C, thus slightly increasing with increasing tempering temperature. The size of coarsest carbides increased more markedly with tempering temperature (see size distributions in Figs 1c,f,i).

The aspect ratio of carbides was determined as the ratio between the maximum and minimum Feret diameters for each particle. For all materials most values ranged between 1 and 3 (Fig. 1j). Their distribution was reasonably fitted by a lognormal distribution function, *F*, described as:

$$F(x) = \frac{1}{\sqrt{2\pi}x\,w}\ exp\left(\frac{-\left(ln\frac{x}{x_c}\right)^2}{2w^2}\right) \quad (4)$$

In Eq. 4, w is a measurement of the broadness of the distribution. The values of x_c and w are indicated for each material in Fig. 1j. Coarser M_3C carbides were more globular in Material C (Fig. 1g) than in Materials A (Fig. 1a) and B (Fig. 1d). Fig. 1 suggests that the highest temper removed most of the needle-like M_3C carbides, as these were scarcely found in Material C.

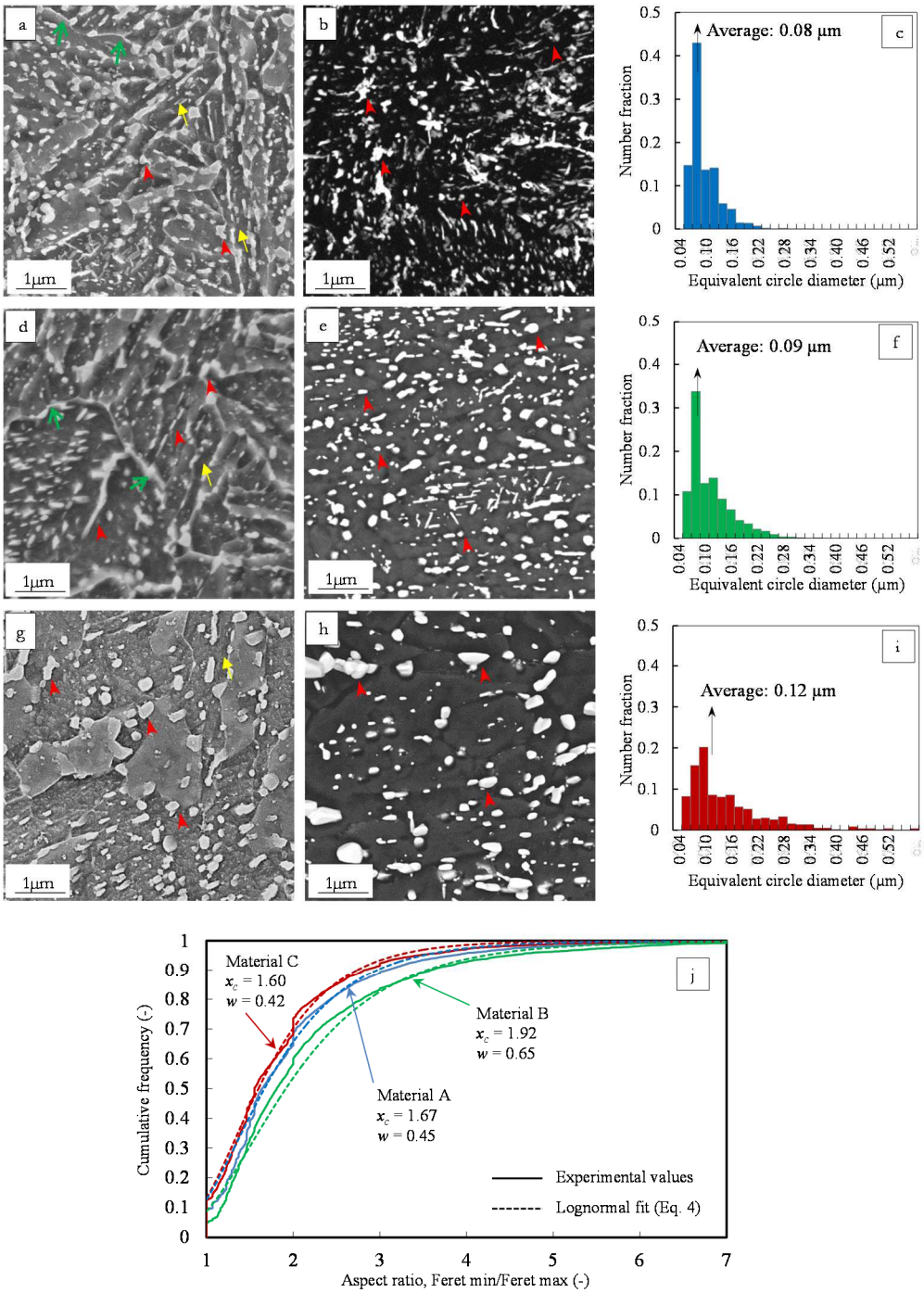

Fig.1. Portion of typical SEM micrographs of bulk samples (a, d, g), replicas (b, e, h), as well as carbide size distributions (c, f, i) for Material A (a-c), Material B (d-f), and Material C (g-i), respectively. (j) Aspect ratio of carbides. The observed plane is perpendicular to the bar axis. Red, yellow and green arrows respectively indicate M_3C carbides, martensite laths and prior austenite grain boundaries.

2.3. Mechanical testing

In order to investigate the role of carbides in the physical ductile fracture mechanism, tensile tests were carried out at room temperature on smooth specimens with 6 mm gauge diameter and 50 mm gauge length. The tensile specimens were cut parallel to the bar axis to minimize the area of manganese sulfide inclusions that were elongated along the rolling direction of the bar. Additional specimens tested along the radial direction (normal to the bar axis) showed early ductile fracture nucleated from the elongated inclusions, i.e., the so-called lamellar tearing well-known for this steel family [8, 11, 21]. As will be shown below and in agreement with [8], specimens tested along the bar axis, i.e., parallel to elongated sulfides and inclusion alignments, showed very little contribution of inclusions in the fracture process. Part of the tests along the bar axis (Material A) has already been reported in [49]. Three specimens of each material were tested at prescribed displacement rate of 0.05 $mm.s^{-1}$, i.e., with an engineering strain rate of 10^{-3} s^{-1}. A longitudinal extensometer of 30 mm in gauge length was used to monitor axial strains.

Measured tensile properties of Materials A, B, and C are reported in Table 2. Material A was strongest, while Materials B and C displayed slightly higher fracture elongation, yet with similar reduction of area at fracture. The higher the tempering temperature, the softer and the more strain-hardenable the martensite microstructure, probably due to both carbide coarsening and matrix recovery, in agreement with literature data [50-52].

2.4. Quantitative fractographic analysis of tensile specimens

Fracture surfaces of the three materials were observed with the same SEM, using in-lens secondary electron imaging. The macroscopic fracture mode was of the well-known "cup-cone" type. The cone zone was formed by shearing during final crack propagation while the cup zone provided information about the first steps of the ductile fracture process. Thus, fractographic analysis focused on the cup zone close to the specimen axis. This region was macroscopically flat and perpendicular to the bar axis and thus, parallel to the plane that was considered for the microstructural quantification reported in section 2.2. As in e.g. [13, 53-56], image analysis was carried out to quantify the fractographic behavior of the three materials. At least seven images at magnification 2×10^4 (pixel size: 5 nm) were taken from different locations in this zone. More than 500 dimples were considered for each material with 0.04 μm as minimum measured dimple size. Usual image processing procedures were employed to determine the equivalent circle diameter of each dimple. Each experimental dimple size distribution was modelled using the lognormal distribution function, F, described in Eq. 4.

Fig.2 shows typical micrographs of fracture surfaces and dimple size distributions for Materials A, B, and C. There were both deep, isolated large dimples (up to several micrometers in size, dark discs in Fig. 2d) and large regions of smaller dimples (grey regions in Fig. 2d). Owing to the orientation of tensile specimens, the contribution of isolated, coarser voids appeared very minor (Fig. 2d) and fine dimples nucleated around carbide particles covered more than 90% of the fracture surface. As a result, only finer dimples are illustrated in Figs 2a-c and will be considered in the following.

Even if the roughness of the fracture surface was not measured (by using e.g. stereological pairs), fractography suggested that the width-to-depth ratio of fine dimples did not significantly depart from unity. Their aspect ratio was close to 1. Yet, it was not measured, as the local surface relief of the fracture surface (Fig. 2d) would induce distortion by the geometrical projection of the real three-dimensional fracture surface perpendicular to the electron beam (and the bar) axis to make SEM pictures. This could explain why aspect ratios of dimples close to 1.6 have been reported (e.g., in [12]); for instance, an aspect ratio

of $\sqrt{2}$ could be induced by projection of a circular dimple in a 45°-tilted fracture surface onto the plane perpendicular to the electron beam. For these reasons, no focus was made on the distribution of dimple aspect ratio in the present work. Accurate chemical analysis of particles inside dimples was not carried out. This would require taking replicas of the fracture surfaces as in [9, 11] - this was not done here. Nevertheless, the size of particles suggests that coarse oxygen- or sulfur-rich inclusions and carbide precipitates were respectively found inside larger and smaller dimples. Curry and Pratt [8] and Hippsley and Druce [12] underlined that ductile fracture of steels containing a significant volume fraction of M_3C carbides (several percent) follows a dual-scale process of void nucleation and coalescence, with large voids forming at inclusions and finer, more numerous voids forming at cementite particles. Such a process was thought to take place in the present work. In summary, it was assumed that M_3C carbide particles observed inside the numerous smaller dimples controlled the ductile fracture process of Materials A, B, and C.

The rounded shape of carbides observed in fractographs (Figs. 2a-c) suggested that nucleation occurred by decohesion at carbide-matrix interfaces, as in e.g. [11, 12], and not by carbide fracture. Due to their low contrast in grey level, it was not possible to automatically detect particles in dimples, so that the distribution of carbide in dimples was not determined as in [12]. Nevertheless, by comparing micrographs and fracture surface pictures (e.g., Figs 1 and 2), the size distribution of carbides found in dimples did not significantly differ from that of carbides measured from carbon replicas. There was at least one carbide per dimple in Materials A and B (Fig. 2a,b), i.e., at least one carbide per half void once fracture had occurred. This suggests that voids could have developed from a set of several (unbroken) carbides in the present case, in particular for Materials A and B. This will be further discussed at the end of the paper. Fig. 2 also provides equivalent circle diameter distributions of dimples; these were well described with a lognormal function (Eq. 4). The average dimple size was increased by 40% with increasing tempering temperature (compare Material A with Material C). Higher dimple size of Materials B and C compared to Material A could be due to a difference in spatial distribution of coarser M_3C carbides, associated to more stable cavity growth before coalescence, and possibly to more extended ductile damage development. To address this assumption, the spatial distribution of carbides was quantified using full-field methods as explained in the next section.

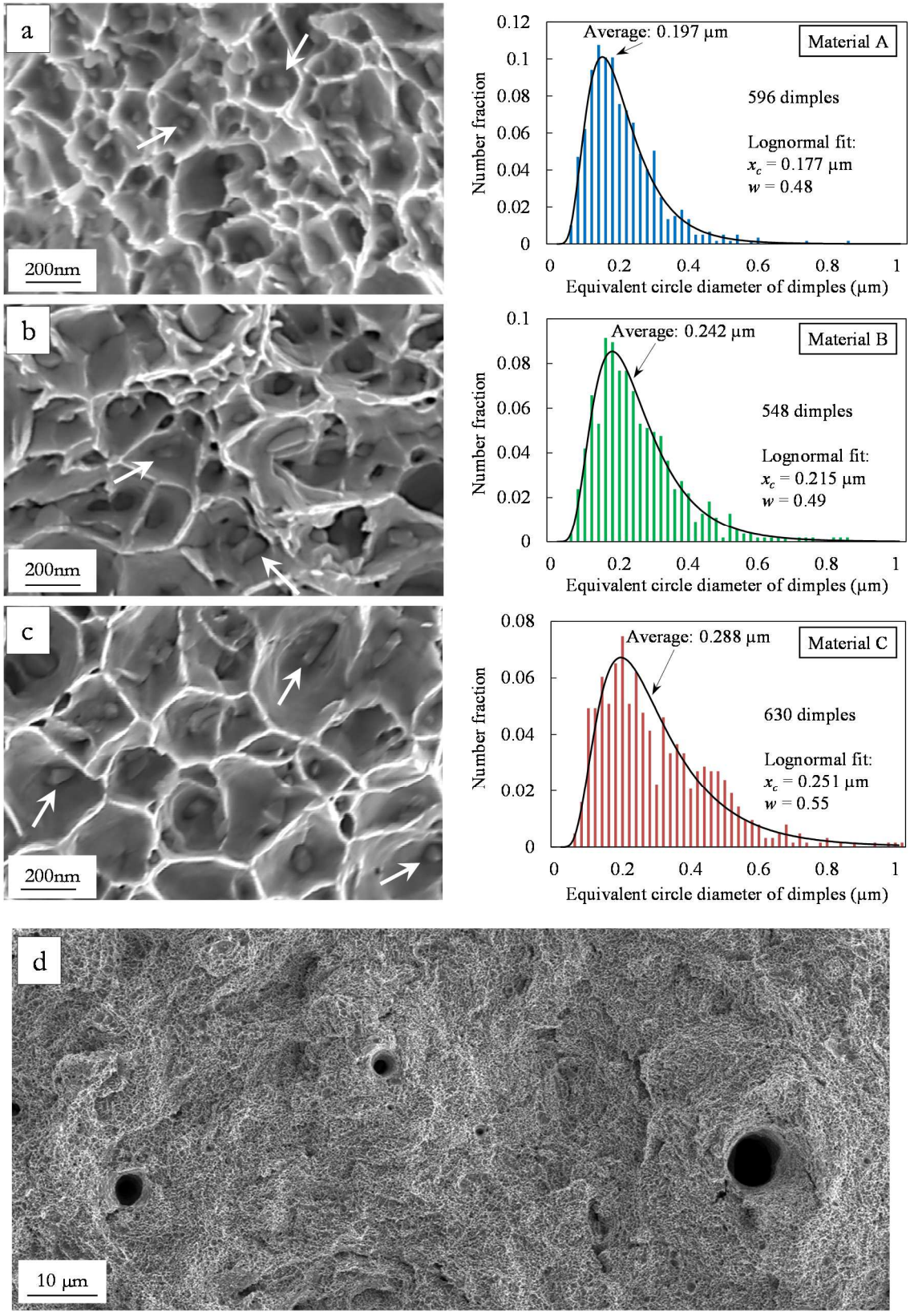

Fig.2. Portions of typical SEM images of fine-dimpled regions of fracture surfaces used for quantitative analysis and equivalent circle diameter distributions of dimples for: a) Material A, b) Material B and c) Material C. Some cementite particles are indicated by arrows. d) Low-magnification view of the fracture surface of Material B showing the minor contribution of larger dimples nucleated from sulfide inclusions (black discs).

3. Image analysis methods

3.1. Image processing

As presented in Fig. 3, the grey level distribution of carbon replica micrographs was bimodal, whereas the broad grey level distribution of SEM micrographs of bulk samples was not favorable to the thresholding operation because of overlapping between peaks from the matrix (darker grey in Fig. 3a) and from the particles (lighter grey in Fig. 3a). Thus, only replica micrographs were used for microstructural image analysis. Binarization of replica micrographs was made using Matlab® software in order to obtain binary images on which quantitative morphological measurements were carried out.

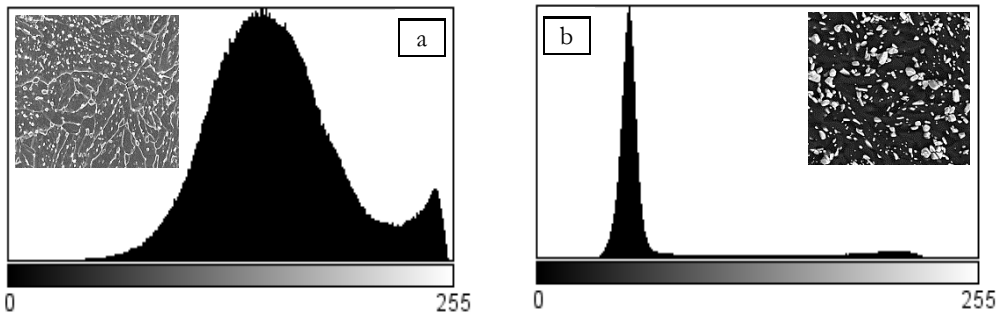

Fig.3. Illustration of the grey level distribution with the corresponding typical SEM micrograph of: a) a bulk sample and b) a replica taken from Material C.

3.2. Position of the theoretical problem

Fig.4 gives an illustration of two objects X_1 and X_2 having x_1, y_1 and x_2, y_2 respectively as the coordinates of their centers of mass. The distance between these objects is denoted as $d(X_1, X_2)$, its definition having to be relevant to the physical phenomena under interest. As for the ductile fracture process, void growth and coalescence into dimples is due to necking of the ligament of matter located between the voids. Even if carbides could be present in that ligament, fracture surfaces strongly suggested that in the investigated steel, many carbide particles acted as void nucleation sites, so that the size of the ligament could be tightly linked to the distance between carbides. As a consequence, analysis focused on the expected width of the ligament, as estimated using the edge-to-edge particle spacing distribution. This required taking the actual shape of objects (here, carbides) into account.

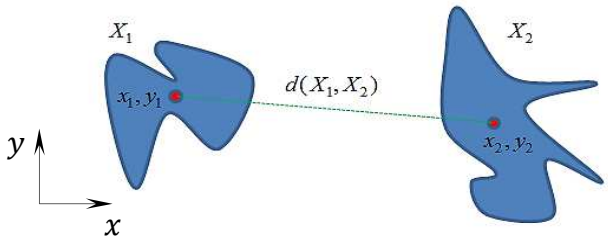

Fig.4. Illustration of the distance between centers of mass of objects X_1 and X_2 (red circles). In this case, the size of these objects is not negligible with respect to the distance between their centers of mass.

In the present case of a dense spatial distribution of medium-sized and irregularly-shaped particles, the selected definition of $d(X_1, X_2)$ was based on mathematical morphology. This scientific field indeed proposes tools allowing appreciation of a so-called "object distance" in an image. The method consists on the establishment of an inter-object (or interparticle) distance map called the "distance function" hereafter.

3.3. Distance function and watershed

The distance function consists in evaluating a Euclidean propagation (like isotropic dilation) from the edge of each particle of a binary image as presented in Fig.5.a. The minimum number of those iterations -yielding the first impingement of the propagated objects- corresponds to the minimum distance between any objects in the image. The distance function allows estimation of the NND between particles, as well as its associated watershed. It was first introduced by Schreiber [57] and the watershed is now largely used for segmentation processes (see e.g. [58]). The formulation is well detailed in Beucher and Lantuéjoul [59]. The watershed has a significant role on localization of particle edges. The continuous version of the distance function has been defined by Schmitt and Mattioli [60] but for the sake of clarity, a discrete approach is used below to explain the principle of the method.

In the morphological approach adopted in the present work, the NND between objects X_1 and X_2 , $d(X_1, X_2)$ is given by the following equation:

$$d(X_1, X_2) = 2 \cdot \inf \{\lambda,\ \delta_\lambda(X_1) \cap \delta_\lambda(X_2) \neq \emptyset\} \quad (5)$$

In Eq. 5, λ refers to each isovalue of the distance obtained after one iteration of the distance function during the dilation of considered particles. $\delta_\lambda(X)$ is the result of the λ–th dilation of object X. The result of the first two iterations is presented in Fig.5.a, where no impingement has occurred yet. The factor 2 is introduced in Eq. 5 in order to allow comparison with distances estimated from the Voronoi tiling algorithm.

For every iteration $\lambda > d(X_1, X_2)/2$ of the propagation process, new impingements may occur between domains $\delta_\lambda(X_1)$ and $\delta_\lambda(X_2)$. For each new impingement point M, the value of λ that produced impingement at point M, λ_M, is recorded. Once the whole image has been filled with propagated objects, the propagation process is stopped. All impingement loci M from all propagation iterations are joined in a continuous set of lines called the "watershed boundaries" of the distance function (white line in Fig.5.b). The distance itself is defined as the *set* of *all* individual values of $2 \cdot \lambda_M$ that have been gathered during the iterative propagation process. Thus the distance between two objects is no longer a single scalar but a distribution of values measured along the watershed boundaries. We define "watershed subsets" (Fig.5.b) as the regions of influence of every particle between the particle edge and the neighboring watershed boundaries. As for the Voronoi tiling algorithm, objects are nearest-neighbors if their watershed subsets share a common boundary. In the Voronoi algorithm, the distance between centers of mass involves one single direction per couple of objects (see dotted line in Fig.4). The distance measured with the watershed-based method involves a variety of directions originating from the propagation process (see green arrows pointing outwards from objects X_1 and X_2 in Fig.5.a).

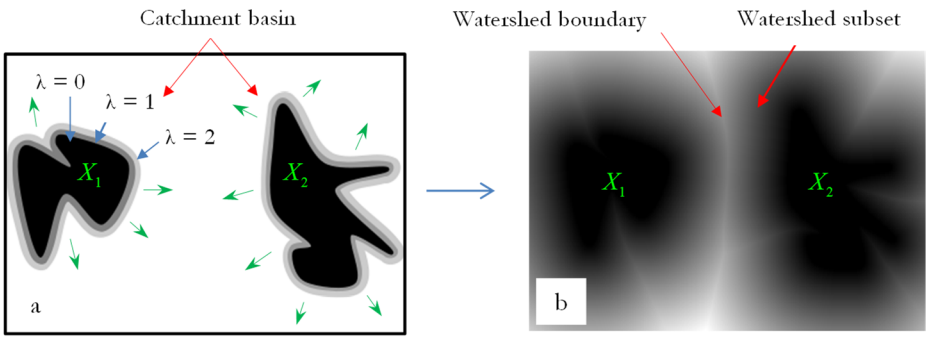

Fig.5. Schematic illustration of the distance function, for a model image with only two objects, a) first two dilations of particles X_1 and X_2 that initiate flooding of catchment basins; b) watershed boundary (white line) and watershed subsets (grey regions) obtained after full completion of the procedure. The darker the grey level, the higher the value of the distance function

3.4. Implementation

The above mentioned method was implemented in Matlab® software and applied to each replica micrograph. Numerical operations of the image analysis tool firstly involved segmentation of carbides by the thresholding operation (section 3.1). Then, the watershed algorithm (section 3.3) was applied. In this work, the selected objects were coarser M_3C carbides and watershed boundaries; they appear in red and light grey, respectively, in the following illustrations. About two minutes were sufficient to apply the numerical analysis tool on more than twenty replica micrographs using a desktop computer.

4. Results of morphological quantification and discussion

4.1. Quantification of the distance between carbides

Both the above-mentioned method based on the watershed algorithm and that based on the classical Voronoi tiling algorithm (as explained in Section 1) were applied, for comparison purposes, on each of the three materials. Typical image processing results are presented in Fig.6. Only portions of actually analyzed images are displayed in Fig.6 in order to make the watershed boundaries more clearly distinguishable to the reader.

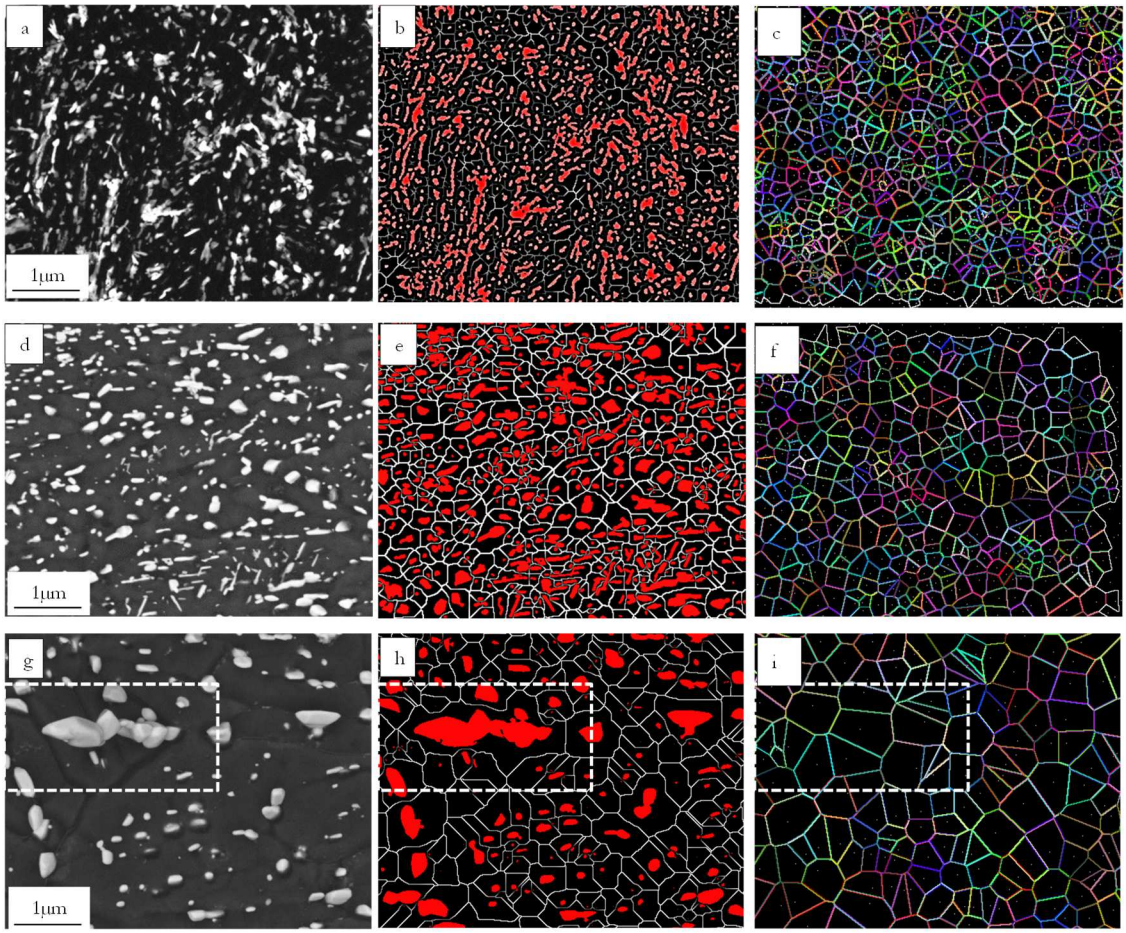

Fig.6. Portions of images of the same region showing (a, d, g) replica micrographs; (b, e, h) segmented carbides (in red) and watershed boundaries (grey lines), and (c, f, i) Voronoi cells, respectively for Material A(a-c), Material B (d-f), and Material C (g-i). Dashed lines indicate the region considered in Fig. 7.

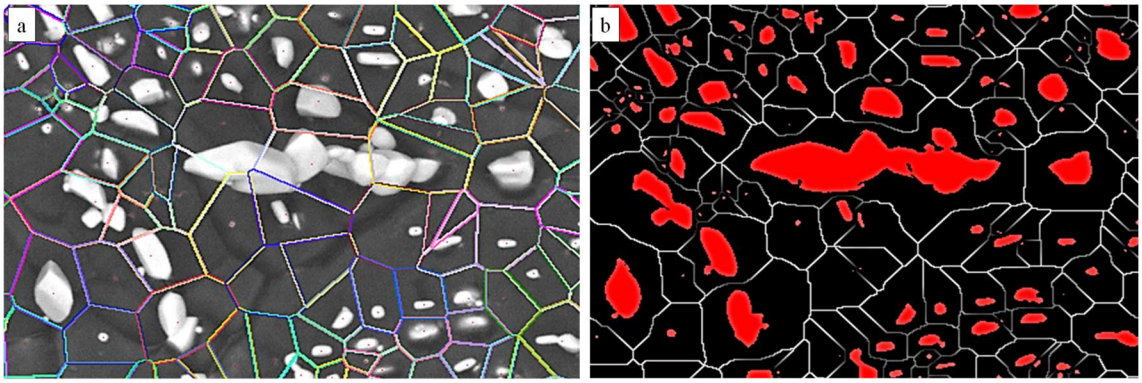

Fig. 7. Illustration of artefacts induced by the Voronoi tiling algorithm in the case of densely distributed particles, in a region taken from Fig. 6g-i. a) Voronoi cells (colored lines) superimposed on the original replica micrograph; centers of mass are indicated by red dots; b) watershed boundaries (grey lines) superimposed on a binned image (particles in red).

Thresholding before applying the watershed-based method allowed satisfactory segmentation of particles. The watershed boundaries are represented using grey lines in Figs. 6(b,e,h) and Fig. 7b. The, Voronoi cells are delimited by color lines in Figs 6(c,f,i) and

Fig. 7a. In contrast to watershed subsets, Voronoi cells only take a convex, polygonal shape (readily visible by comparison between e.g. Fig. 6h and Fig 6i. for Material C). Moreover, the Voronoi tiling algorithm does not take the shape of particles into account. Owing to the high fraction of carbides, particles are even not necessarily enclosed inside the Voronoi cell generated from their own center of mass (see the central particle in Fig. 7). When the particle size is locally small compared to interparticle spacing, watershed subsets and Voronoi cells take similar shapes (see e.g. the two tiny particles below the central one in Fig. 7). In the present work, the watershed-based method seems to better represent the microstructure of the three materials. The number of individual values of carbide spacing measured per micrograph was at least 50,000 and 450 by the watershed-based and the Voronoi-based methods, respectively. Namely, the Voronoi-based method only considered NNDs between centers of mass of carbides [31]. On the other hand, the watershed method kept the entire set of values along the watershed boundaries (one value per pixel along the lines of Figs 6(b,e,h) and Fig. 7b). This allows a more comprehensive geometrical characterization of matrix ligaments between carbides. As a result, the statistical database provided by the watershed-based method appears richer in view of the ductile fracture process.

The results of statistical analysis obtained with the two methods are given in Fig. 8 and Table 3. First, the plots of Figs 8a-c are compared to each other, for a given quantification method. The minimum values were similar for all watershed-based results. The higher the tempering temperature, the broader the distribution (see the factor two between values of w). This could be due to some spatial heterogeneity in the carbide coarsening process that is expected to take place during the additional tempering step applied to Materials B and C. As a consequence, the experimental average value of carbide spacing was higher by 40% for Material C compared to Material A.

In all three materials, Voronoi-based distributions were well described using the lognormal function defined by Eq. 4 (Fig. 8). Watershed-based distributions only fairly agreed with their lognormal fit. Due to the high frequency of lower values, they appeared more symmetrical than their Voronoi-based counterparts determined from the *same* segmented micrographs. This shows that even the mathematical function that describes interparticle spacing distributions is sensitive to the image analysis method.

The minimum values of carbide spacing given by the Voronoi method (0.03 μm) are much higher than those of minimum in-plane thickness of matrix ligaments as revealed by the watershed method (0.015 μm) (Fig. 8). Both were smaller than the minimum size of carbides (0.05 μm). By considering edge-to-edge measurements instead of NNDs between centers of mass, the watershed-based method caught lower values of carbide spacing; these values were actually present in the material. This difference is readily visible because of the high density of carbides: the size of ligaments is of the same order as the size of particles itself. These thin matrix regions, which are better characterized using the watershed-based method than by the Voronoi method, is expected to influence local void coalescence during ductile damage development.

To more accurately compare carbide spacing distributions obtained with the two methods, the size of carbides may be taken into account in several simple manners in further analysis of Voronoi-based results. First, one can subtract the maximum size of carbides, C_{max}, from the largest values of carbide spacing calculated using the Voronoi algorithm, V_{max}. This yields Voronoi-based estimate of the larger edge-to-edge distance between carbides, $V_{max} - C_{max}$. By doing this, one makes the reasonable assumption that larger carbides are surrounded by a larger carbide-free region, due to pumping of carbon atoms from the solid solution during carbide coarsening; this assumption is in agreement with observations (Fig.

1 g-h). Estimates of C_{max} were taken from the tail of the carbide size distributions (Fig. 1) but excluding the few highest values to avoid sampling artefacts. To this aim, C_{max} was defined as the 95th percentile of the size distribution. From Table 3, the values of V_{max} - C_{max} are obviously much smaller than largest values of carbide spacing obtained using the watershed algorithm, W_{max}. Higher values of the watershed distance function may arise from e.g. strongly non-convex particles (see e.g. the upper-right part of Fig. 5b), for which a high number of iterations is locally necessary to flood the catchment basin. On the other hand, except for Material A, subtracting the average value of the carbide size, C_{ave}, from the Voronoi-based distribution rather well agrees with the watershed-based distribution up to about the 50th percentile (Figs 8b, 8c, and right part of Table 3). This agrees with the qualitative observation that carbides closer to each other could be of any size in the micrographs (see e.g. Fig. 6d). It means that no obvious correlation exists between individual size and distances between carbides, except for the coarsest ones (see e.g. Fig. 6g).

Material	Maximum values of morphological parameters (µm)				Average values of morphological parameters (µm)			
	Carbide size (C_{max})	Spacing, Voronoi (V_{max})	V_{max} - C_{max}	Spacing, watershed (W_{max})	Carbide size (C_{ave})	Spacing, Voronoi (V_{ave})	V_{ave} - C_{ave}	Spacing, watershed (W_{ave})
A	0.16	0.37	0.21	0.62	0.08	0.16	0.08	0.14
B	0.25	0.59	0.34	0.65	0.09	0.27	0.18	0.17
C	0.33	1.04	0.71	1.20	0.12	0.43	0.31	0.32

Table 3. Comparison between maximum (respectively, average) spacing between carbides measured using the watershed method and those obtained with the Voronoi tiling method, from which maximum (respectively, average) values of carbide sizes were subtracted.

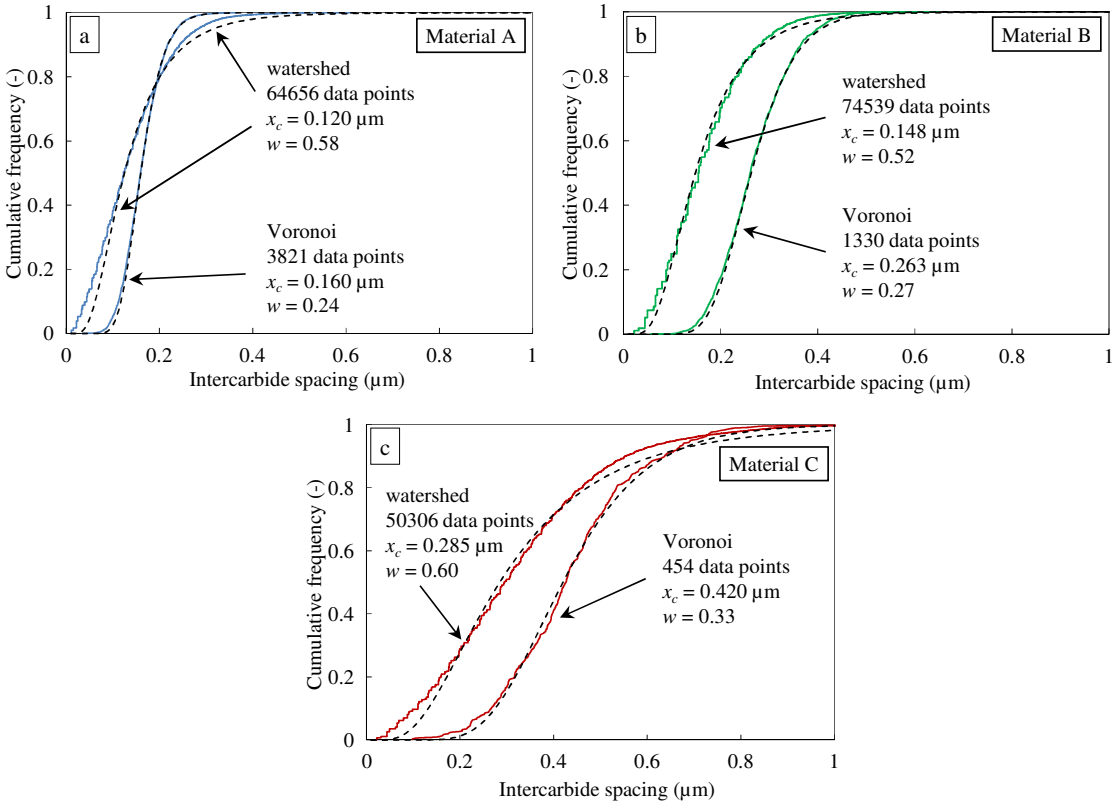

Fig.8. Carbide spacing distributions respectively obtained by the developed watershed tool and the Voronoi tiling algorithm for a) Material A, b) Material B and c) Material C. Continuous lines: experimental data points; dashed lines: lognormal fits using Eq. 4.

4.2. Comparison between carbide spacing and dimple size distributions

In literature, average values of dimple size have already been compared to microstructural features affecting void nucleation such as intersections of slip lines or deformation-induced martensite with grain boundaries [55, 61]) and second phase particles in aluminum and magnesium alloys [9, 62]. Dimple size distributions have also been reported in α/β zirconium alloys [56] but not related to the distribution of void-nucleating α/β interfaces. As for bcc iron alloys, dimple size distributions have been reported in HSLA steels [53, 54] and in quenched and tempered steels [1, 12]. All of them appeared asymmetrical but none of them was described with a mathematical distribution function.

To the authors' knowledge, no comparison *between statistical distributions of both dimple size and particle spacing* is available from open literature in martensitic steels. Such a comparison is available for casting aluminum alloys [58], yet with little void growth from fractured silicon particles. As for steels, only average values of dimple size and particle spacing were compared in [8, 11, 12]. One-to-one correspondence between dimple and nucleating particle has been reported in [1, 12, 13] focusing on a growth ratio between dimple size and particle size. Such a ratio may also be derived from average values of particle and dimple size [11]. This ratio was close to 1 in some instances indicating little cavity growth before coalescence [8, 11, 12] but much higher growth ratios (2.5-6) have also been reported [1, 12, 13].

In the present work, experimental distributions of dimple size and carbide spacing are compared in Fig.9 for the three materials. First of all, the distributions of dimple size and carbide spacing range over similar values, whatever the considered material. This agrees with reports on ductile fracture of 300M high-strength steel once carbide-matrix interface had been weakened by phosphorus segregation [12]. A similar result was also reported for a spheroidized steel [8], and for 0.36C-Cr-Ni quenched and tempered steel in the case of tensile tests [1], all of them breaking with fine dimples nucleated at carbides.

Let us now compare the shape of dimple size and particle spacing distributions. The only case where carbide spacing well matches the dimple size distribution, both in absolute value and in shape, is found for the watershed-based distribution in Material C (Fig. 9c). It is worth noting that the shape of dimple size distribution was not correlated at all to that of the Voronoi-based carbide spacing. In Material A, the dimple size distribution is rather parallel to the watershed-based one, the difference being close to the average carbide size (80 nm, Fig. 1c). This is also true (yet to a lesser extent) for Material B. In Material C, the dimple size distribution was close to that of carbide spacing obtained using the watershed method. As a whole, dimple size distributions were parallel to those of the watershed based values, at least in their upper parts (typically, from the 40th percentile). The lower parts were not really parallel. As mentioned before, the dimple size distributions were well described by a lognormal function, whereas the watershed distributions were more symmetrical. A possible explanation is that carbides located close to each other did not lead to well-separated dimples. Voids located between them probably impinged very early in the fracture process, leading to a unique dimple with several carbides inside, as illustrated by the white arrow in Fig. 2a. As a whole, the watershed method seems to provide better comparison of statistical distribution of particles spacing and of ductile fracture dimples.

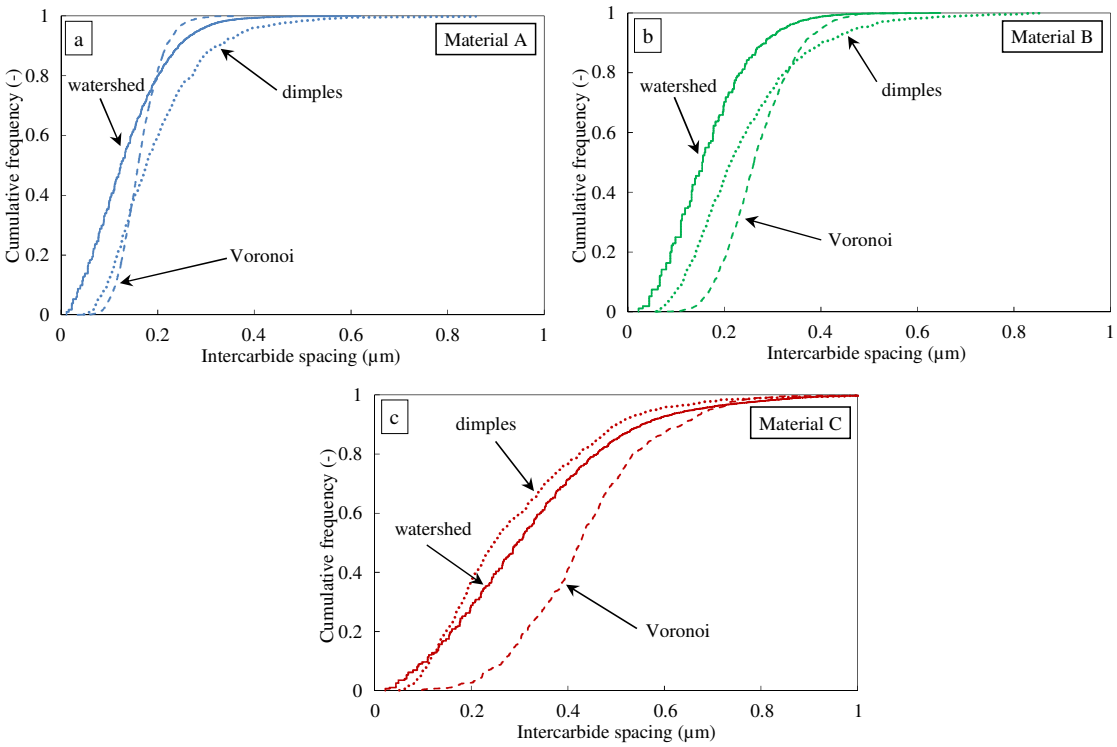

Fig.9. Comparison between experimental carbide spacing and dimple size distributions for a) Material A, b) Material B and c) Material C.

What appears to be good agreement between dimple size and watershed-based particle spacing distributions actually originates from combined contributions of a number of physical phenomena that occur during ductile fracture, namely:

i. The reduction of area at fracture ranged between 60% and 70% (see Section 2.3). As fracture surfaces were mainly circular, in-plane strain close to about 30% can be expected perpendicular to the tensile axis. The ratio between axial and radial spacing of voids varies with strain in a complex manner in the general case of a non-random spatial distribution of voids [20] but the evolution of radial spacing itself is not addressed in [20]. In the present work, it is supposed that the axial strain tends to reduce the carbide spacing compared to those measured by image analysis of non-deformed material. This contribution could not be accurately assessed, as the etching behavior of the material right under the fracture surface was unstable, leading to high tendency to carbide clustering; quantitative analysis of replicas (taken from that region) was thus not possible.

ii. As illustrated in Fig. 2, at least one carbide was found in most dimples, which means that at least two carbides were involved in the void development process in most cases (carbide fracture was only scarcely found). In addition, not all carbides in a given plane did nucleate an individual cavity. This tends to reduce the number density of dimples and thus, to increase their size for a given carbide spacing distribution.

iii. While carbide spacing distributions were assessed within a very shallow region perpendicular to the bar axis, namely, the etched volume of metallographic samples, ductile fracture actually involved a larger volume [35], which, in the case of pronounced necking observed here, was much larger than that involved in

microstructural quantification. Carbides that contributed to ductile fracture were not necessarily located within the plane of maximum diameter reduction, even in the cup region of the fracture surface. This tends to shift the dimple size distribution toward lower values.

Contributions of closely-spaced carbides (ii) and from non-planar damage development and ductile cracking (iii) were further assessed by observing longitudinal cross-sections prepared with conventional polishing followed by a colloidal silica finish. The same SEM was used as previously described, using backscattered electron imaging (Fig. 10). The spatial extent of the damaged region was very limited, over a distance to the fracture surface of 10 μm, 60 μm, and 80 μm for Materials A, B, and C, respectively. So, it was not possible to quantify the void fraction as a function of strain (as measured from diameter reduction) as classically done for materials that develop ductile damage over a large volume [11, 14, 15, 39, 43]. Especially for Material A, void coalescence probably occurred very rapidly after void nucleation, whereas for Materials B and C, limited stable cavity growth seemed to occur. In all three materials, fracture occurred well before void nucleation could happen over a large portion of the necking region.

The rather equiaxed shape of voids in Fig. 10 is consistent with the equiaxed shape of dimples in Figs 2 a-c. On the other hand, fracture surfaces were macroscopically flat but pronounced relief appeared at the microscopic scale, Fig. 10. Yet, dimples appeared as "closed" objects rather equiaxed in shape (Fig. 2); this would not be the case if shear fracture were responsible for the majority of the fracture surface, as in the "cone" part of the cup-cone morphology. Moreover, stress triaxiality develops in the central part of the necking region. Consequently, mode I (opening) cracking is thought to significantly contribute to the fracture process in the investigated specimens. For a tilt angle of 45°, the distortion resulting from the projection of the real three-dimensional surface onto a two-dimensional SEM picture can be estimated using a circular dimple shape of diameter D_{3D}. In that case, the projection leaves one diameter unchanged (the one parallel to the tilt axis). On the SEM picture, it multiplies the perpendicular diameter by $\cos(45°) = 2^{-0.5}$, as well as the area of the projected dimple. As a result, the equivalent circle diameter of the ellipsoid in the image picture, D_{2D}, is equal to $2^{-0.25} \cdot D_{3D} \approx 0.84 \cdot D_{3D}$. In other words, D_{3D} is close to $1.19 \cdot D_{2D}$. This projection-induced artefact thus induces an underestimate of the real equivalent circle diameter of the dimple by about 20%. This does not significantly affect the above comparison between dimple size and carbide spacing distributions.

In cross-sections, one carbide only was observed close to every small (freshly nucleated) void but cavity growth parallel to the tensile axis could eventually link two aligned carbides (see e.g. the arrow in Fig. 10b). This phenomenon has already been reported in literature (e.g. [14, 25, 39]). It could explain the high fraction of dimples containing at least one carbide (Fig. 2). This would not be due to carbide fracture during the nucleation stage, but to the cavity growth process.

In Material A (Fig. 10a), fracture came with very limited spatial extent of damage development. Only very small cavities were found next to the fracture surface and no coalescence was observed out of the fracture surface itself. Several tiny carbides were found in many dimples (Fig. 2) but most carbide particles were inactive in the cavity development process, suggesting a significant contribution of (ii) but a probably limited contribution of (iii). As a whole, the dimple size distribution well correlated with the distribution of local in-plane ligament thickness, once corrected by taking the carbide size into account (as previously mentioned).

In Material C (Fig. 10c), damage was found over an extended volume, so that the propagating crack could scan a large population of voids and thus, contribution (iii) was expected to be more effective. One carbide was still found per dimple in many cases, and not all carbides triggered void nucleation (Fig. 10c), so that contribution (ii) was probably lower than in Material A, but sill significant. Contribution (i) was the same as for Material A (same reduction of area at fracture). As a result (Fig. 9c), the dimple distribution was close to the watershed-based carbide spacing distribution.

In the intermediate case of Material B, both contributions (ii) and (iii) were expected to be effective. There was at least one particle per dimple as for Material A, whereas the extent of damage development (60 μm) ranged between the cases of Materials A (10 μm) and C (80 μm), respectively (Fig. 10b). As a result, the dimple size distribution was roughly parallel to that of the watershed carbide spacing, but the difference between them, in particular for the 0-20th percentile range, was smaller than the average carbide size (0.09 μm, Fig. 1b).

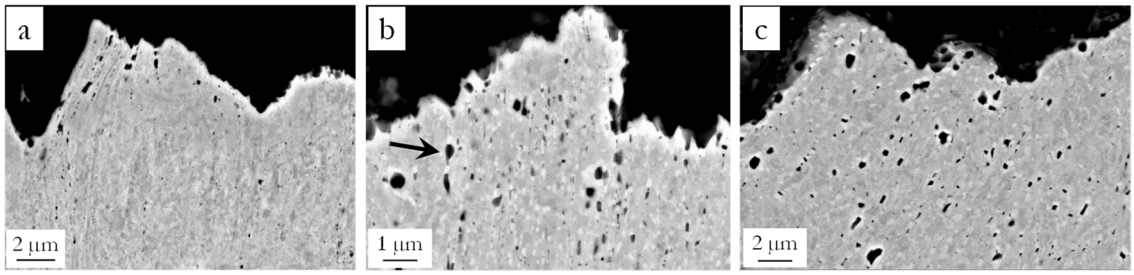

Fig.10. Longitudinal cross-sections showing ductile damage close to the fracture surfaces of a) Material A, b) Material B and c) Material C. Backscattered electron imaging. The tensile axis is vertical. Voids and carbides respectively appear in black and in white. The arrow points toward a cavity nucleated at a carbide (located at its top part) and growing toward the bottom part of the picture, eventually meeting another carbide particle, at which another cavity had also nucleated.

The relevance of watershed-based measurements to ductile fracture investigations deserves more detailed analysis, involving micromechanical assessment of deformation of ligaments between growing micro-voids. This, in turn, involves a strong competition between strain localization (prominent in Material A) and more generalized void nucleation and growth (more visible in Material C). Such an analysis requires detailed descriptions of the work-hardening behavior of the martensite matrix under complex stress states [63]; this was out of scope of the present work. In a more simple and qualitative manner, the shape of individual dimples may be compared to that of watershed subsets. In particular, rather isolated alignments of carbides (e.g. in the central part of Fig. 6g-h) yielded anisotropic watershed subsets with boundaries perpendicular to those alignments (and thus, parallel to each other). Similar shapes were found in some regions of the fracture surface (e.g., under the left arrow in Fig. 2a). The low values of the distance function at these boundaries suggest early coalescence of these cavities by internal necking along the direction of particle

alignment; further growth of the resulting larger, elongated cavity then occurred up to final fracture. Qualitatively, cavity growth ended up earlier at thinner regions of ligaments, both for geometrical reasons (internal necking occurring earlier) and for mechanical reasons (stress in these regions being probably very high). This is well accounted for by the watershed method, but not at all by the Voronoi tiling algorithm.

5. Conclusions

A new image processing tool based on the watershed method was developed and used for the estimation of the edge-to-edge carbide spacing distribution, by automatically taking the shape of individual particles into account. The results were compared with those of the Voronoi method, as well as with the size distribution of ductile dimples on the fracture surface. This work led to the following conclusions:

- Once implemented, the watershed-based method readily provided a rich set of data, namely, a distribution of in-plane thickness of ligaments whose deformation is necessary to void growth during ductile fracture. This distribution was broader than that given by the Voronoi tiling algorithm.
- The mathematical description of carbide spacing distributions was sensitive to the image analysis method. In the present work, the Voronoi-based dataset was much better fitted to a lognormal distribution than the watershed-based one (that was more symmetrical).
- Except for Material A having the finest microstructure, the lower values of carbide spacing were not experimentally correlated to the size of involved carbides, so that the first 50% of the watershed distribution could be satisfactorily approximated by subtracting the average carbide size from the Voronoi-based distribution.
- Comparison of watershed-based distributions, dimple size distributions, as well as fractography and damage analysis qualitatively revealed the combined contributions of void development (eventually involving more than one carbide per cavity) and out-of-plane damage development. The watershed method appears as a promising tool to be used with micromechanical modelling of ductile damage development in alloys containing a high density of hard particles such as carbides.

Acknowledgements

This work was financially supported by the French Innovation Supporting Agency (ANRT) under Grant CIFRE 2016/0670. Kind help from A. Hermant and B. Raviart (Centre des Matériaux) for setting up the replica preparation method is gratefully acknowledged.

Data availability statement

The raw/processed data required to reproduce these findings cannot be shared at this time as the data also forms part of an ongoing study.

References

[1] A. N. Kumar and R. K. Pandey, Effect of inclusions and states of stress on the mechanics of fracture in quenched and tempered Ni-Cr-Mo steel, Mater. Sci. Eng. 63 (1984) 121–136. https://doi.org/10.1016/0025-5416(84)90169-1

[2] E. Chang, C.Y. Chang, C.D. Liu, The effects of double austenitization on the mechanical properties of a 0.34C containing low-alloy Ni-Cr-Mo-V steel, Metall. Mater. Trans. 25A (1994) 545-555. https://doi.org/10.1007/BF02651596

[3] G. Krauss, Heat Treated Martensitic Steels: Microstructural Systems for Advanced Manufacture, ISIJ Int. 35 (1995) 349-359. https://doi.org/10.2355/isijinternational.35.349

[4] S.K. Dhua, D. Mukerjee, D.S. Sarma, Effect of cooling rate on the as-quenched microstructure and mechanical properties of HSLA-100 steel plates, Metall. Mater. Trans. 34A (2003) 2495-2504. https://doi.org/10.1007/s11661-003-0009-0

[5] P. Michaud, D. Delagnes, P. Lamesle, M.H. Mathon, C. Levaillant, The effect of the addition of alloying elements on carbide precipitation and mechanical properties in 5% chromium martensitic steels, Acta Mater. 55 (2007) 4877-4889. https://doi.org/10.1016/j.actamat.2007.05.004

[6] A. Salemi, A. Abdollah-zadeh, The effect of tempering temperature on the mechanical properties and fracture morphology of a NiCrMoV steel, Mater. Charact. 59 (2008) 484-487. https://doi.org/10.1016/j.matchar.2007.02.012

[7] J. Feng, M. Wettlaufer, Plane-strain fracture toughness of AISI 4140 steel austempered below M_S, Mater. Sci. Eng. A743 (2019) 794-799. https://doi.org/10.1016/j.msea.2018.11.122

[8] D. A. Curry and P. L. Pratt, The Role of Second Phase Particles in the Ductile Fracture of Higher Carbon Steels, Mater. Sci Eng. 37 (1979) 223–235. https://doi.org/10.1016/0025-5416(79)90156-3

[9] D. Broek, The role of inclusions in ductile fracture and fracture toughness, Eng. Fract. Mech. 5 (1973), 55-66. https://doi.org/10.1016/0013-7944(73)90007-6

[10] A. S. Argon, J. Im, R. Safoglu, Cavity formation from inclusions in ductile fracture, Metall. Trans. 6A (1975) 825-837. https://doi.org/10.1007/BF02672306

[11] T.B. Cox, J.R. Low, Jr., An investigation in the plastic fracture of AISI 4340 and 18 Nickel-200 grade maraging steels, Metall. Trans. 5 (1974) 1457-1470. https://doi.org/10.1007/BF02646633

[12] C. A. Hippsley and S. G. Druce, The influence of phosphorus segregation to particle/matrix interfaces on ductile fracture in a high strength steel, Acta Metall. 31 (1983) 1861–1872. https://doi.org/10.1016/0001-6160(83)90132-3

[13] W.M. Garrison, Jr, N. R. Moody, The influence of inclusion spacing and microstructure on the fracture toughness of the secondary hardening steel AF 1410, Metall. Mater. Trans. 18A (1987) 1257-1263. https://doi.org/10.1007/BF02647195

[14] D. Kwon, R.J. Asaro, A study of void nucleation, growth, and coalescence in spheroidized 1518 steel, Metall. Mater. Trans. 21A (1990) 117-134. https://doi.org/10.1007/BF02656430

[15] A. A. Benzerga, J. Besson, A. Pineau, Anisotropic ductile fracture Part I: experiments, Acta. Mater. 52 (2004) 4623-4638. https://doi.org/10.1016/j.actamat.2004.06.020

[16] T.C. Lindley, G. Oates, G.E. Richards, A critical appraisal of carbide cracking in ferrite/carbide aggregates, Acta Metall. 18 (1970) 1127-1136. https://doi.org/10.1016/0001-6160(70)90103-3

[17] K.-H. Schwalbe, On the influence of microstructure on the crack propagation mechanisms and fracture toughness of metallic materials, Eng. Fract. Mech. 9 (1977) 795-832. https://doi.org/10.1016/0013-7944(77)90004-2

[18] S.H. Goods, L. M. Brown, Overview No.1: The nucleation of cavities by plastic deformation, Acta Metall. 27 (1979) 1-15. https://doi.org/10.1016/0001-6160(79)90051-8

[19] M.N. Shabrov, A. Needleman, An analysis of inclusion morphology effects on void nucleation, Modelling Simul. Mater. Sci. Eng. 10 (2002) 163-183. https://doi.org/10.1088/0965-0393/10/2/305

[20] A.A. Benzerga, Micromechanics of coalescence in ductile fracture, J. Mech. Phys. Solids 50 (2002) 1331-1362. https://doi.org/ 10.1016/S0022-5096(01)00125-9

[21] G. R. Speich, W. A. Spitzig, Effect of volume fraction and shape of sulfide inclusions on through-thickness ductility and impact energy of high-strength 4340 plate steels, Metall. Trans. 13A (1982) 2239-2258. https://doi.org/10.1007/BF02648395

[22] D.M. Goto, D.A. Koss, V. Jablokov, The influence of tensile stress states on the failure of HY-100 steel, Metall. Trans. 30A (1999) 2835-2842. https://doi.org/10.1007/s11661-999-0121-x

[23] V. Jablokov, D.M. Goto, D.A. Koss, J.B. McKirgan, Temperature, strain rate, stress state and the failure of HY-100 steel, Mater. Sci. Eng. A302 (2001) 197-205. https://doi.org/10.1016/S0921-5093(00)01832-3

[24] U. F. Kocks, On the spacing of dispersed obstacles, Acta Metall. 14 (1966) 1629–1631. https://doi.org/10.1016/0001-6160(66)90185-4

[25] C.T. Liu, J. Gurland, The fracture behavior of spheroidized carbon steels, Trans. ASM 61 (1968) 156-167. (no doi found)

[26] M.F. Ashby, R. Ebeling, On the determination of the number, size, spacing, and volume fraction of spherical second-phase particles from extraction replicas, Trans. Metall. Soc. AIME 236 (1966) 1396-1404. (no doi found)

[27] M. Ashby, The hardening of metals by non-deforming particles, Z. Metallkunde 55 (1964) 5-17. (no doi found)

[28] S. Lee, S. Kim, B. Hwang, B. S. Lee, and C. G. Lee, Effect of carbide distribution on the fracture toughness in the transition temperature region of an SA 508 steel, Acta Mater. 50 (2002) 4755–4762. https://doi.org/10.1016/S1359-6454(02)00313-0

[29] E. E. Underwood, Quantitative Stereology for Microstructural Analysis," in Microstructural Analysis: Tools and Techniques, J. L. McCall and W. M. Mueller, Eds. Boston, MA: Springer US, 1973, pp. 35–66.

[30] F. Aurenhammer, Voronoi Diagrams—a Survey of a Fundamental Geometric Data Structure. ACM Computing Surveys 3 (1991) 345–405. https://doi.org/10.1145/116873.116880

[31] L. Burtseva, B. Valdez Salas, F. Werner, and A. Pestryakov, Voronoi diagrams and tessellation methods for modeling the material structure, Appl. Mech. Mater. 756 (2015) 426-435. https://doi.org/10.4028/www.scientific.net/AMM.756.426

[32] C. Stone and I. Tsakiropoulos, Characterisation of spatial distribution of reinforcement in powder metallurgy route Al/SiCp metal matrix composites Part 1 - Techniques based on microstructure, Mater. Sci. Technol. 11 (1995) 213-221. https://doi.org/10.1179/mst.1995.11.3.213

[33] J. Lemaitre, A continuous damage mechanics model for ductile fracture, J. Eng. Mater. Technol. 107 (1985) 83-89. https://doi.org/10.1115/1.3225775

[34] A. Das, T. Chowdhury, S. Tarafder, Ductile fracture micro-mechanisms of high strength low alloy steels, Mater. Des. 54 (2014) 1002-1009. https://doi.org/10.1016/j.matdes.2013.09.018

[35] J. R. Rice and D. M. Tracey, On the ductile enlargement of voids in triaxial stress fields, J. Mech. Phys. Solids. 17 (1969) 201–217. https://doi.org/10.1016/0022-5096(69)90033-7

[36] J. Gurland, J. Plateau, The mechanism of ductile rupture of metals containing inclusions, Trans. ASM 56 (1963) 442-454. (no doi found)

[37] A. R. Rosenfield, G. T. Hahn, Linear arrays of moving dislocations piling-up against an obstacle, Acta Metall. 16 (1968) 755-759. https://doi.org/10.1016/0001-6160(68)90147-8

[38] L.M. Brown, W.M. Stobbs, The work-hardening of copper-silica V. Equilibrium plastic relaxation by secondary dislocations. Philos. Mag. 34 (1976) 351-372. https://doi.org/10.1080/14786437608222028

[39] G. Le Roy, J. D. Embury, G. Edwards, M. F. Ashby, A model of ductile fracture based on the nucleation and growth of voids, Acta Metall. 29 (1981) 1509-1522. https://doi.org/10.1016/0001-6160(81)90185-1

[40] W. M. Garrison, Jr, N. R. Moody, Ductile Fracture, J. Phys. Chem. Solids 48 (1987) 1035-1074. https://doi.org/10.1016/0022-3697(87)90118-1

[41] F. A. McClintock, A criterion for ductile fracture by the growth of holes, J. Appl. Mech. 35 (1968) 363-371. https://doi.org/10.1115/1.3601204

[42] A. L. Gurson, Continuum theory of ductile rupture by void nucleation and growth: Part I—Yield criteria and flow rules for porous ductile media, J. Eng. Mater. Technol. 99 (1977) 2-15. https://doi.org/10.1115/1.3443401

[43] M. A. Greenfield, H. Margolin, The mechanism of void formation, void growth, and tensile fracture in an alloy consisting of two ductile phases, Metall. Trans. 3 (1972) 2649-2659. https://doi.org/10.1007/BF02644241

[44] A. A. Benzerga, J. Besson, A. Pineau, Anisotropic ductile fracture Part II: theory, Acta. Mater. 52 (2004) 4639-4650. https://doi.org/10.1016/j.actamat.2004.06.019

[45] K. E. Puttick, Ductile fracture in metals, Philos. Mag. 4 (1959) 964-969. https://doi.org/10.1080/14786435908238272

[46] V. Tvergaard, A. Needleman, Analysis of the cup-cone fracture in a round tensile bar, Acta Metall. 32 (1984) 157-169. https://doi.org/10.1016/0001-6160(84)90213-X

[47] J. P. Bandstra, D. A. Koss, Modeling the ductile fracture process of void coalescence by void-sheet formation, Mater. Sci. Eng. A319–321 (2001) 490-495. https://doi.org/10.1016/S0921-5093(00)02007-4

[48] J. Besson, Damage of ductile materials deforming under multiple plastic or viscoplastic mechanisms, Int. J. Plast. 25 (2009) 2204-2221. https://doi.org/10.1016/j.ijplas.2009.03.001

[49] F. Tioguem, M. Mazière, F. Tankoua, A. Galtier, A.F. Gourgues-Lorenzon, Identification of ductile to brittle transition temperature by using plane strain specimen in tensile test and correlation with instrumented Charpy impact test: experimental and numerical study, Mechanics and Industry 19 (2018) 107-117. https://doi.org/10.1051/meca/2017034

[50] N. Ridley, S. Maropoulos, and J. D. H. Paul, Effects of heat treatment on microstructure and mechanical properties of Cr–Mo–3·5Ni–V steel, Mater. Sci. Technol. 10 (1994) 239–249. https://doi.org/10.1179/mst.1994.10.3.239

[51] Y. Tomita, Low- Temperature improvement of mechanical properties of AISI 4340 steel through high-temperature thermomechanical treatment, Metall. Trans. 22A (1991) 1093–1102. https://doi.org/10.1007/BF02661103

[52] B. M. Strauss, Quantitative Methods in Fractography. ASTM International, 1990.

[53] A. Das, S. K. Das, S. Sivaprasada, S. Tarafder, Fracture-property correlation in copper-strengthened high-strength low-alloy steel, Scr. Mater. 59 (2008) 681-683. https://doi.org/10.1016/j.scriptamat.2008.05.043

[54] A. Das, S. K. Das, S. Tarafder, Correlation of Fractographic Features with Mechanical Properties in Systematically Varied Microstructures of Cu-Strengthened High-Strength Low-Alloy Steel, Metall. Mater. Trans. 40A (2009) 3138-3146. https://doi.org/10.1007/s11661-009-9999-6

[55] A. Das, S. Tarafder, Experimental investigation on martensitic transformation and fracture morphologies of austenitic stainless steel, Int. J. Plast. 25 (2009) 2222-2247. https://doi.org/10.1016/j.ijplas.2009.03.003

[56] Z.N. Yang, F.C. Zhang, L. Qu, Z.G. Yan, Y.Y. Xiao, R.P. Liu, X.Y. Zhang, Formation of duplex microstructure in Zr–2.3Nb alloy and its plastic behaviour at

various strain rates, Int. J. Plast. 54 (2014) 163-177. http://dx.doi.org/10.1016/j.ijplas.2013.08.013

[57] A. Schreiber, Didaktische Schriften zur Elementarmathematik. Logos Verlag Berlin GmbH, 2014. ISBN 978-3-8325-3716-6

[58] A. Kruglova, M. Roland, S. Diebels, T. Dahmen, P. Slusallek, F. Mücklich, Modelling and characterization of ductile fracture surface in Al-Si alloys by means of Voronoi tessellation, Mater. Charact. 131 (2017) 1-11. https://dx.doi.org/10.1016/j.matchar.2017.06.013

[59] S. Beucher and C. Lantuéjoul, Use of watersheds in contour detection, Int. Workshop Image Process. Real-Time Edge Motion Detect., p. 2.1-2.12, Jan. 1979.

[60] M. Schmitt and J. Mattioli, Morphologie mathématique. Paris: Masson, 1994. ISBN-13: 978-2225843853

[61] T. G. Nieh, W. D. Nix, A comparison of the dimple spacing on intergranular creep fracture surfaces with the slip band spacing for copper, Scr. Metall. 14 (1980) 365-368. https://doi.org/10.1016/0036-9748(80)90360-9

[62] C. D. Calhoun, N. S. Stoloff, The effects of particles on fracture processes in magnesium alloys, Metall. Trans. 1 (1970) 997-1006. https://doi.org/10.1007/BF02811784

[63] C. Tekoğlu, J.W. Hutchinson and T. Pardoen, On localization and void coalescence as a precursor to ductile fracture, Philos. Trans. R. Soc. A373 (2015) 20140121. http://doi.org/10.1098/rsta.2014.0121